Simultaneous Car-Borne SAR Imaging at L-Band and Ku-Band for DInSAR-Based Mobile Mapping of Ground Motion in Alpine Terrain

Othmar Frey[a,b], Charles Werner[a], and Rafael Caduff[a]
[a]Gamma Remote Sensing, Gümligen, Switzerland
[b]ETH Zurich, Switzerland

Abstract

In this contribution, we present high-resolution car-borne DInSAR imagery of a fast-moving landslide, simultaneously acquired at Ku-band and L-band. Recently, we have developed and implemented a car-borne—and UAV-borne—DInSAR end-to-end system at L-band also including INS/GNSS-based navigation, SAR focusing, and interferometric processing. Using this L-band SAR system we have demonstrated car-borne and UAV-borne measurements of ground motion at various sites. We then enhanced the car-based setup by adding a Ku-band SAR system alongside the Gamma L-Band SAR. In October 2023, we revisited the Brinzauls landslide in Switzerland, where we acquired high-resolution car-borne repeat-pass DInSAR data at Ku-band and L-band. This active landslide consists of various compartments with different kinematic behavior and with different land cover. Our car-borne DInSAR imagery obtained at Ku-band and L-band provides critical information at high spatial resolution to localize and distinguish landslide compartments moving at different velocities for a more detailed mapping of geological-kinematic features within the landslide.

1 Introduction

Over the last few years, we have established a car-borne and UAV-borne DInSAR end-to-end system at L-band including radar instrumentation, INS/GNSS-based navigation, SAR focusing, and interferometric processing. Using this novel mobile mapping system we have successfully demonstrated car-borne and UAV-borne measurements of ground motion / slope stability and glacier flow velocity at various sites [1, 2]. Recently, we have augmented the car-borne measurement setup by also adding a Ku-band SAR system [3, 4, 5] next to the Gamma L-Band SAR system (see **Tables 1 & 2** and **Fig. 1**). First results of this dual-frequency setup, which allows imaging of a scene simultaneously at both frequencies were reported in [6, 7]. In October 2023, we revisited the Brinzauls landslide [8] in Switzerland after a large mass movement event that had occurred in June 2023 —see also [2], where we reported on L-band-only car-borne mobile mapping of ground motion of the same landslide. The Brinzauls landslide is an active landslide that consists of several compartments, the mechanism and movement of which are only partially understood. Also, the landslide includes various types of land cover, including open escarpments and debris, vegetated areas, including meadows and forests, as well as buildings and roads. High-resolution imaging of ground motion at the two frequencies (Ku-band and L-band) can therefore provide critical information to discriminate features and bodies moving at different velocities. In this paper, we present high-resolution car-borne DInSAR results obtained at Ku-band and L-band, which have been used to map geological-kinematic features within the active landslide.

Table 1 GPRI-based Ku-band SAR specifications

Frequency within	17.1 - 17.3 GHz
used center freq.	17.2 GHz
Chirp bandwidth	50 - 200 MHz
range res. (@200 MHz BW)	0.75 m
Azim. res. (@ full SA)	$\leq$ 0.1 m
Azim. res. (@ SA=100m, R=3km)	$\leq$ 0.3 m
Type	FMCW
Chirp lengths	250 μs - 8 ms.
ADC sampling rate	6.25 MHz
Elev. beamwidth (3dB)	25.0 deg
Azim. beamwidth (3dB)	12.5 deg

Table 2 Gamma L-band SAR specifications

Frequency within	1.2 - 1.4 GHz
used center freq.	1.325 GHz
Chirp bandwidth	50 - 200 MHz
range res. (@100 MHz BW)	1.5 m
Azim. res. (@ full SA)	$\leq$ 0.5 m
Azim. res. (@ SA=100m, R=3km)	2.3 m
Type	FMCW
Chirp lengths	250 μs - 8 ms.
Elev. beamwidth (3dB)	40.0 deg
Azim. beamwidth (3dB)	40.0 deg

ISBN 978-3-8007-6286-6 / ISSN 2197-4403

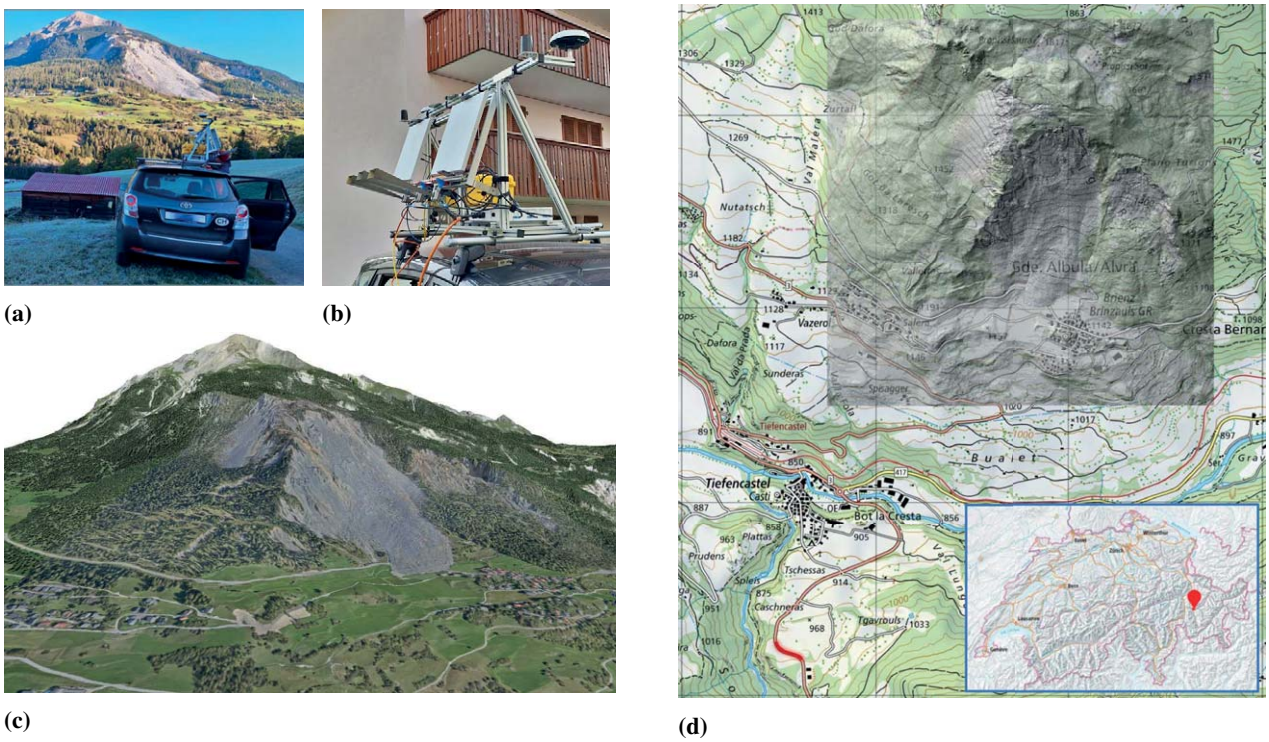

Figure 1 Dual-frequency car-borne DInSAR measurement setup (a) with a view to the Brinzauls landslide from the opposite side of the valley nearby the road section, where the SAR measurements are taken, and (b) a close-up photo. The setup includes a Gamma L-band SAR [1, 2] and a modified Ku-band GPRI [3, 4] in SAR mode with one transmit and two receive Horn antennas. SAR imagery can be acquired simultaneously with both FMCW SAR systems. For accurate positioning a Honeywell HGuide n580 INS/GNSS system with a local GNSS reference station is used. (c) 3-D rendering of the Brinzauls landslide and surroundings after the large mass movement in June 2023. (d) Map overview. (2023 high-res. orthophoto and lidar DEM by Helimap SA, surrounding orthophoto, DEM and map: swissimage, swissAlti3D, Swiss map: © swisstopo).

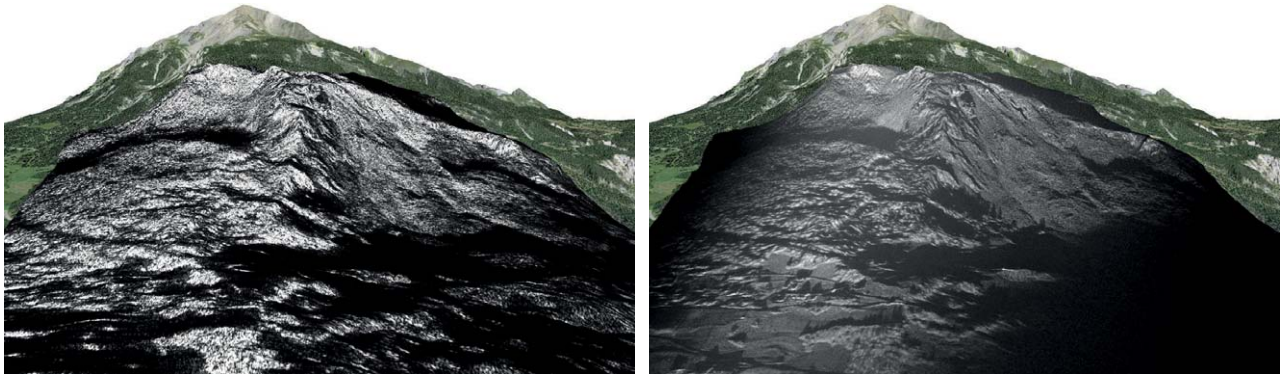

Figure 2 (a) Car-borne L-band SAR image and (b) high-resolution car-borne Ku-band SAR image of the scene.

2 Methods and Data

In **Fig 1**, the dual-frequency car-borne DInSAR setup is shown in front of the area of interest and with a close-up view. The setup includes a Gamma L-band SAR system [1, 2] and a modified Ku-band GPRI [3, 4] in SAR mode with one transmit and two receive Horn antennas. SAR imagery can be acquired simultaneously with both FMCW SAR systems. For accurate positioning a Honeywell HGuide n580 INS/GNSS system with a local GNSS reference station is used. **Tables 1 & 2** list the main specifications of the two SAR systems, the modified GPRI Ku-band SAR system [3, 4, 5, 9] and the Gamma L-band SAR. A time-domain back-projection (TDBP) SAR processor [10, 11, 12, 13] parallelized for NVIDIA GPUs [14] is used to focus the SAR data. A high-resolution digital elevation model derived from airborne laser scanning, acquired after the large landslide in June 2023, as well as post-processed kinematic (PPK) GNSS positions fused with INS data (Honeywell HGuide n580) are used to establish a

ISBN 978-3-8007-6286-6 / ISSN 2197-4403

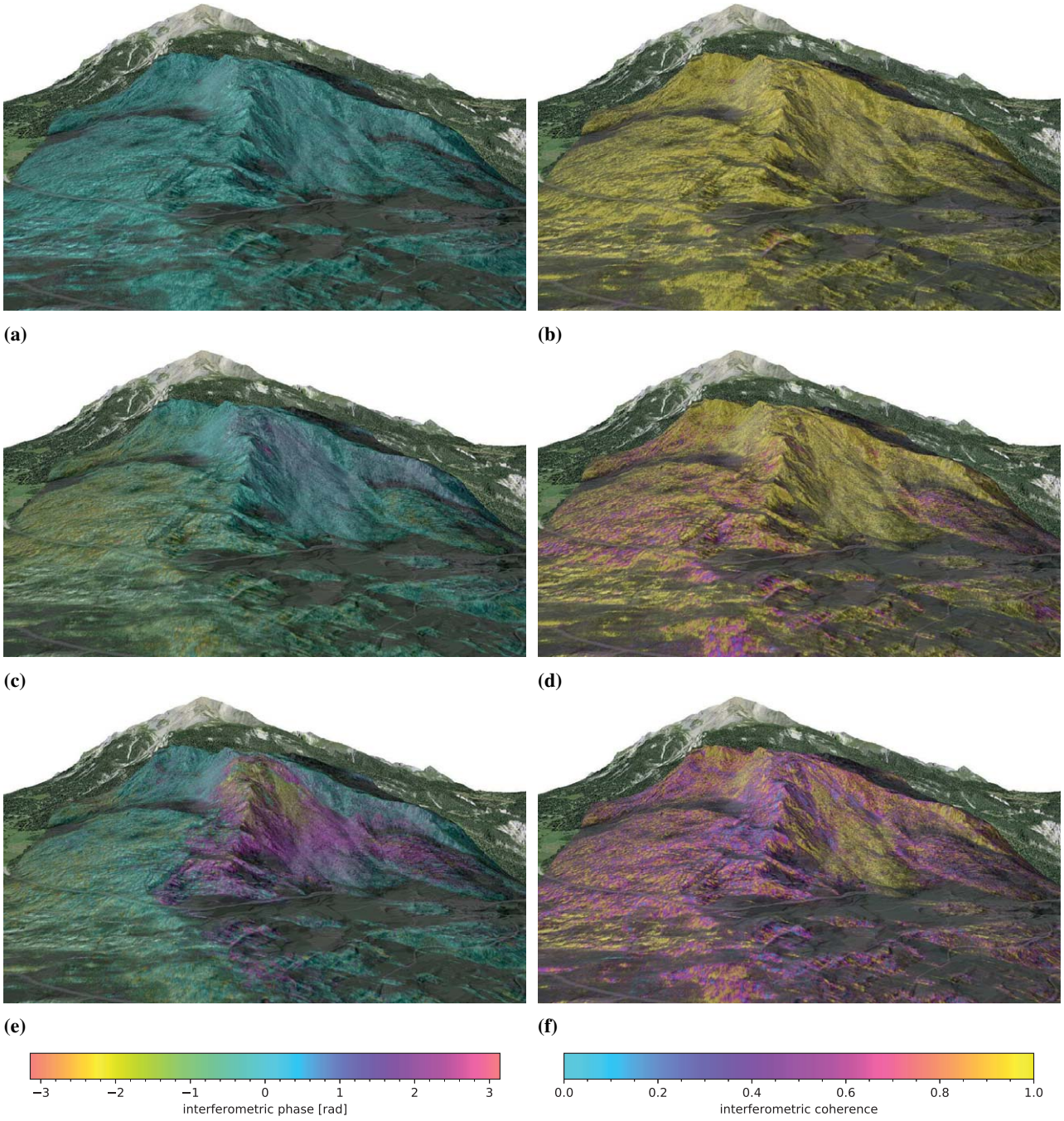

Figure 3 High-resolution car-borne repeat-pass interferometric phase and coherence maps at **L-band** of the Brinzauls landslide for 3 different time intervals: short-term (2.5min interval on 2023-10-16) phase (a) and coherence (b), 1-day (2023-10-16 to 17) repeat-pass interferometric phase (c) and coherence (d), and 7-days (2023-10-16 to 23) repeat-pass interferometric phase (e) and coherence (f). Interferograms and coherence maps are blended with the backscatter intensity map for visualization purposes. The SAR imagery is processed onto a high-resolution digital elevation model. (Auxiliary data: see caption of **Fig.1)**

highly accurate replica of the 3-D radar acquisition geometry which is then used in the TDBP SAR processor. The resulting images and interferograms shown in this paper have not been further corrected or detrended.

3 Results

In **Fig. 2**, high-resolution car-borne SAR intensity images of the Brinzauls landslide taken at L- and Ku-band and processed with TDBP (see Section 2) are shown. In **Fig. 3**, short-term (2.5min), 1-day, and 7-days interferometric phase and coherence maps are shown for repeated car-borne SAR acquisitions at L-band, and in **Fig. 4**, short-term (2.5min), 1-day, and 7-days interferometric phase and coherence maps obtained with the car-borne Ku-band SAR system are shown. In **Fig. 5(a)**, a zoomed view of a 1-day Ku-band interferogram obtained with the car-borne system at range distances of 2-3km away from the escarpment is

ISBN 978-3-8007-6286-6 / ISSN 2197-4403

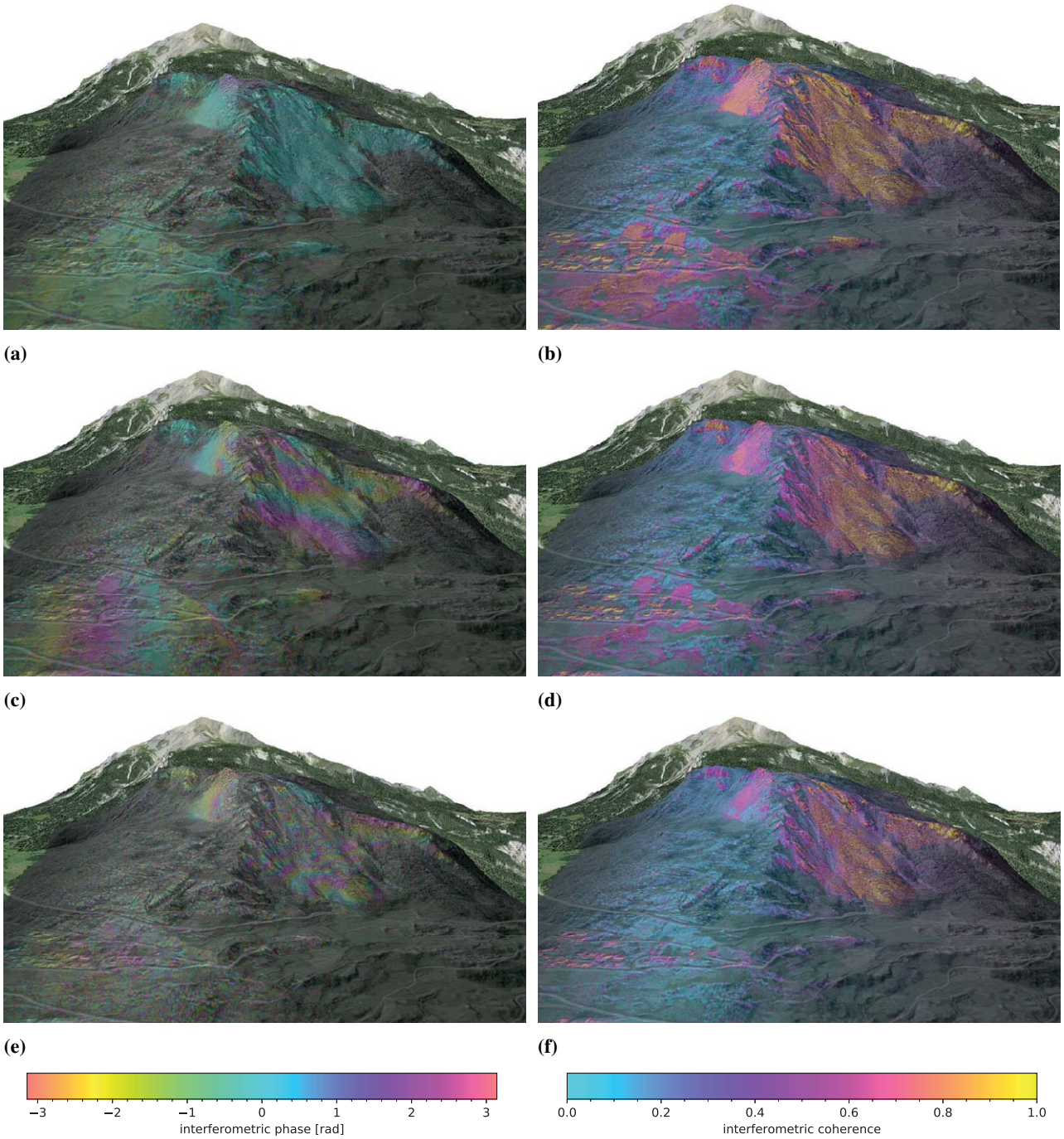

Figure 4 High-resolution car-borne repeat-pass interferometric phase and coherence maps at **Ku-band** of the Brinzauls landslide for 3 different time intervals: short-term (2.5min interval on 2023-10-16) phase (a) and coherence (b), 1-day (2023-10-16 to 17) repeat-pass interferometric phase (c) and coherence (d), and 7-days (2023-10-16 to 23) repeat-pass interferometric phase (e) and coherence (f). Interferograms and coherence maps are blended with the backscatter intensity map for visualization purposes. The SAR imagery is processed onto a high-resolution digital elevation model. (Auxiliary data: see caption of **Fig.1)**

depicted. To illustrate the much-improved azimuth resolution obtained with the car-borne SAR system, a 2-day interferogram of the same area acquired with a rotational-scanning Ku-band GPRI radar placed less than 100 m away at the foot of the debris cone of the mass movement event in June 2023 is given in **Fig. 5(b)**.

4 Discussion

The Ku-band SAR system ($\lambda_{Ku} = 1.74\,cm$) is about 13 times more sensitive to line-of-sight ground motion, spatiotemporal variation of tropospheric path delays, and residual positioning errors than the L-band SAR system ($\lambda_L = 22.6\,cm$) as can readily be observed by comparing the car-borne temporal interferograms at L-band in **Fig. 3**

ISBN 978-3-8007-6286-6 / ISSN 2197-4403

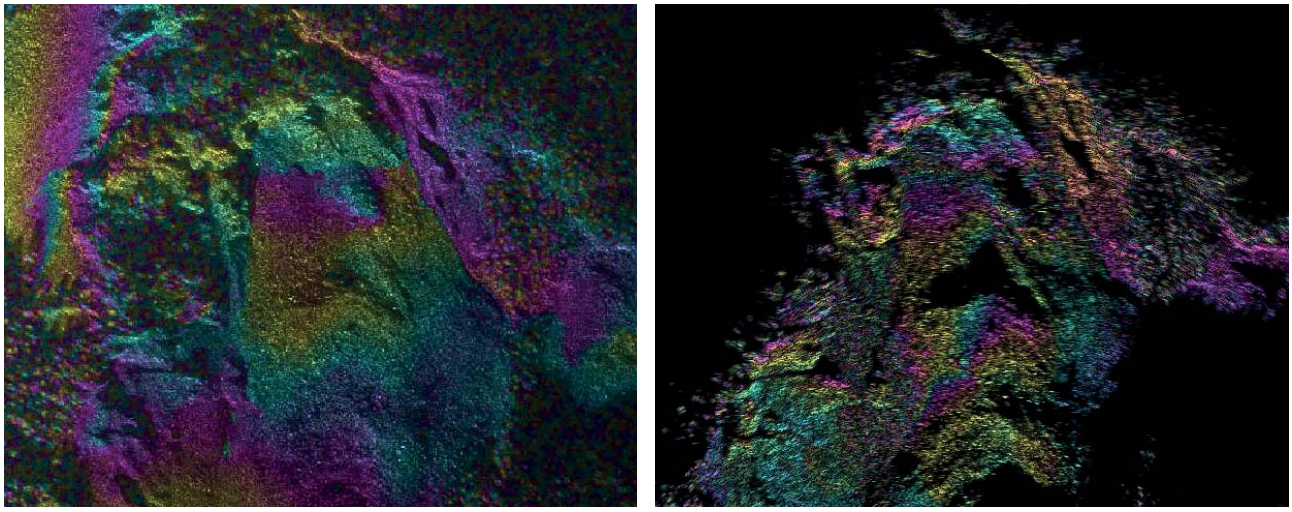

(b)

Figure 5 Zoomed map view of (a) a 1-day car-borne SAR interferogram at Ku-band and (b) a 2-day real-aperture radar interferogram at Ku-band taken with the GPRI (stationary mount point, rotational scanning in azimuth). A much better spatial resolution and a more synoptic view of the landslide is obtained with the car-borne SAR measurements. (The interferometric phases cannot be compared directly since acquisition time, time interval, as well as the view directions do not match.)

and at Ku-band in **Fig. 4**. An important consequence is that at Ku-band subtle displacements already lead to a distinct interferometric phase, such that lines between different compartments of the landslide can already be distinguished at Ku-band after 1-day in our example. On the other hand, the L-band system allows observing ground motion with a larger coverage (besides the escarpment including also vegetated/forested areas) and over longer time intervals (7 days, in this case), thus providing complementary information in areas and over time spans, for which the interferograms at Ku-band are decorrelated.

Particularly, at the Brinzauls landslide observed in this case study, a landslide that has repeatedly experienced large variations of ground motion with substantial accelerations before large mass movement events, measurements at complementary wavelengths, such as Ku- and L-band can be very useful to assess the ground motion more comprehensively. A downside of the good phase sensitivity at Ku-band is that the interferometric phase is also very sensitive towards nuisance signals such as tropospheric path delay and residual positioning errors (as well as errors in the digital elevation model): the short-term (2.5min interval) interferogram at Ku-band **Fig. 4** reveals subtle phase trends mostly in the vegetated areas with lower coherence and towards the southwestern part, whereas the bare rock and soil of the escarpment does not show a significant phase variation over this short time interval, which indicates that residual positioning errors play a minor role in this case. At L-band (see **Fig. 3**) the short-term interferogram shows excellent phase stability and high coherence. At longer time intervals, the atmospheric signal leads to substantial phase trends at Ku-band, which together with the motion-induced phase, yield wrapped phases as can be observed in the 1-day and 7-day interferograms. By contrast, the interferometric phase signal at L-band is easy to interpret even after 7-days and a reasonable level of coherence allows obtaining a more synoptic assessment of the ground motion even in partially vegetated areas.

The high-resolution Ku-band interferograms permit detecting individual features and lines separating different bodies in the landslide moving at different velocities even though the trajectory of observation is 2-3 km away. The improvement in terms of spatial resolution associated with the much better azimuth resolution of the vehicle-based SAR system is remarkable compared to the stationary Ku-band system (see **Fig. 5(a)** and **Table 1**; the azimuth resolution of the stationary GPRI Ku-band radar is 6.8m at 1km distance). In this particular case, an additional advantage of the car-borne measurement site on the opposite side of the valley at a distance of 2-3 km is a more synoptic view of the landslide, which also includes the western flank. While the azimuth resolution obtained with the L-band system is about 1.5-3 meters, an added value is that sufficient coherence is also obtained in parts of the forested and vegetated areas. This permits tracking the slower movements over several days as prevalent particularly in the lower Western side of the active landslide, which is covered by vegetation. These areas are already decorrelated at Ku-band within one day.

5 Conclusion

This case study at the Brinzauls landslide in Switzerland demonstrates that the car-borne mobile mapping DInSAR system, particularly at Ku-band, provides additional high-resolution information to distinguish compartments that move at different velocities; information, which is crucial to improve the geological understanding and modeling of the landslide. In addition, the car-borne SAR measurements at L-band allow tracking ground motion also in veg-

ISBN 978-3-8007-6286-6 / ISSN 2197-4403

etated areas. The dual-frequency car-borne SAR system is therefore suitable for a very detailed landslide assessment at high spatial resolution while the stationary terrestrial interferometric radar systems are the main tool for continuous and operational monitoring at short time intervals at a somewhat limited spatial resolution in azimuth.

Acknowledgment

The car-borne SAR interferometry campaign at Brinzauls was co-funded by CSD Engineers AG.

References

[1] O. Frey, C. L. Werner, and R. Coscione, "Car-borne and UAV-borne mobile mapping of surface displacements with a compact repeat-pass interferometric SAR system at L-band," in *Proc. IEEE Int. Geosci. Remote Sens. Symp.*, 2019, pp. 274–277.

[2] O. Frey, C. L. Werner, A. Manconi, and R. Coscione, "Measurement of surface displacements with a UAV-borne/car-borne L-band DInSAR system: system performance and use cases," in *Proc. IEEE Int. Geosci. Remote Sens. Symp.* IEEE, 2021, pp. 628–631.

[3] C. L. Werner, A. Wiesmann, T. Strozzi, A. Kos, R. Caduff, and U. Wegmuller, "The GPRI multi-mode differential interferometric radar for ground-based observations," in *Proc. EUSAR 2012*, Apr. 2012, pp. 304–307.

[4] T. Strozzi, C. L. Werner, A. Wiesmann, and U. Wegmuller, "Topography mapping with a portable real-aperture radar interferometer," *IEEE Geosci. Remote Sens. Lett.*, vol. 9, no. 2, pp. 277–281, Mar. 2012.

[5] R. Caduff, A. Kos, F. Schlunegger, B. W. McArdell, and A. Wiesmann, "Terrestrial radar interferometric measurement of hillslope deformation and atmospheric disturbances in the Illgraben debris-flow catchment, Switzerland," *IEEE Geoscience and Remote Sensing Letters*, vol. 11, no. 2, pp. 434–438, Feb. 2014.

[6] O. Frey, C. Werner, and R. Caduff, "Dual-frequency car-borne DInSAR at L-band and Ku-band for mobile mapping of surface displacements," in *Proc. of EUSAR 2022 - 14th European Conference on Synthetic Aperture Radar*. VDE Verlag GmbH, July 2022, pp. 489–492.

[7] O. Frey, C. Werner, and R. Caduff, "Car-borne mobile mapping of ground motion by means of repeat-pass SAR interferometry: Case studies and application development based on L-band and Ku-band SAR data acquisitions," in *Proc. IEEE Int. Geosci. Remote Sens. Symp.* Pasadena: IEEE, July 2023, pp. 1902–1905.

[8] D. Figi, R. Thöny, T. Breitenmoser, F. Brunold, and T. Schwestermann, "Rutschung Brienz/Brinzauls (GR): Geologisch-kinematisches und hydrologisches Modell," *Swiss Bull. angew. Geol.*, vol. 27, no. 2, pp. 17–34, 2022.

[9] R. Caduff, F. Schlunegger, A. Kos, and A. Wiesmann, "A review of terrestrial radar interferometry for measuring surface change in the geosciences," *Earth Surface Processes and Landforms*, vol. 40, no. 2, pp. 208–228, 2015.

[10] O. Frey, C. Magnard, M. Rüegg, and E. Meier, "Focusing of airborne synthetic aperture radar data from highly nonlinear flight tracks," *IEEE Trans. Geosci. Remote Sens.*, vol. 47, no. 6, pp. 1844–1858, June 2009.

[11] A. Ribalta, "Time-domain reconstruction algorithms for FMCW-SAR," *IEEE Geosci. Remote Sens. Lett.*, vol. 8, no. 3, pp. 396–400, May 2011.

[12] C. Stringham and D. G. Long, "GPU processing for UAS-based LFM-CW stripmap SAR," *Photogrammetric Engineering & Remote Sensing*, vol. 80, no. 12, pp. 1107–1115, 2014.

[13] O. Frey, C. L. Werner, U. Wegmuller, A. Wiesmann, D. Henke, and C. Magnard, "A car-borne SAR and InSAR experiment," in *Proc. IEEE Int. Geosci. Remote Sens. Symp.*, 2013, pp. 93–96.

[14] O. Frey, C. L. Werner, and U. Wegmuller, "GPU-based parallelized time-domain back-projection processing for agile SAR platforms," in *Proc. IEEE Int. Geosci. Remote Sens. Symp.*, July 2014, pp. 1132–1135.

ISBN 978-3-8007-6286-6 / ISSN 2197-4403